



# Synthesis of $\text{In}_2\text{S}_3$ and $\text{Ga}_2\text{S}_3$ crystals for oxygen sensing and UV photodetection



Ching-Hwa Ho<sup>a,b,\*</sup>, Min-Han Lin<sup>a</sup>, Yi-Ping Wang<sup>b</sup>, Ying-Sheng Huang<sup>b</sup>

<sup>a</sup> Graduate Institute of Applied Science and Technology, National Taiwan University of Science and Technology, Taipei 106, Taiwan

<sup>b</sup> Graduate Institute of Electro-Optical Engineering and Department of Electronic and Computer Engineering, National Taiwan University of Science and Technology, Taipei 106, Taiwan

## ARTICLE INFO

### Article history:

Received 9 November 2015

Received in revised form 6 April 2016

Accepted 1 May 2016

Available online 4 May 2016

### Keywords:

$\text{In}_2\text{S}_3$

Oxygen sensing

$\text{Ga}_2\text{S}_3$

Optoelectronic property

## ABSTRACT

Crystal growth, characterization, and sensing application of  $\text{In}_2\text{S}_3$  and  $\text{Ga}_2\text{S}_3$  are demonstrated herein. Single crystals of  $\text{In}_2\text{S}_3$  and  $\text{Ga}_2\text{S}_3$  were grown by chemical vapor transport method using  $\text{ICl}_3$  as the transport agent. The as-grown  $\text{In}_2\text{S}_3$  crystals essentially show dark red and  $\text{Ga}_2\text{S}_3$  displays transparent and light-yellow colored. X-ray diffraction measurements show tetragonal phase of the as-grown  $\text{In}_2\text{S}_3$  crystals while  $\text{Ga}_2\text{S}_3$  crystallizes in the monoclinic structure. The optical band edges of  $\text{In}_2\text{S}_3$  and  $\text{Ga}_2\text{S}_3$  were characterized by absorption and thermoreflectance measurements. The optical band gaps of  $\text{In}_2\text{S}_3$  and  $\text{Ga}_2\text{S}_3$  are 1.935 eV and 3.052 eV, respectively. The direct gaps of  $\text{In}_2\text{S}_3$  and  $\text{Ga}_2\text{S}_3$  lie in between red to violet visible region. Photoluminescence (PL) experiments characterize defect and surface-state emissions of the  $\text{In}_2\text{S}_3$  and  $\text{Ga}_2\text{S}_3$  crystals. The  $\text{In}_2\text{S}_3$  can easily form surface oxide in environmental air with an  $\text{In}_2\text{O}_3$  growth rate of  $\sim 100$  nm/day (i.e. for oxygen sensing). The PL intensity of the  $\text{In}_2\text{O}_3$  formed on  $\text{In}_2\text{S}_3$  may be a sensing index for oxygen content detection. Besides,  $\text{Ga}_2\text{S}_3$  may emit a broadened visible white light (near band edge) due to the existence of intrinsic defects inside the crystal. The  $\text{Ga}_2\text{S}_3$  crystal also displays a high-sensitivity photoconductivity change illuminated by a 405 nm laser. According to the experimental results,  $\text{In}_2\text{S}_3$  can be an oxygen sensor with the formation of surface oxide (i.e.  $\text{In}_2\text{O}_3$ ), while  $\text{Ga}_2\text{S}_3$  may possess potential capability in fabrication of blue to UV photodetector.

© 2016 Elsevier B.V. All rights reserved.

## 1. Introduction

Recently the demands on energy-related and environmental friendly materials are raised significantly because the purpose of green power, ambient control, optoelectronics, and medical uses. III–VI (III = Ga, In, and VI = S, Se) semiconductors are well-known defect crystals with many promising applications in solar-cell material (e.g.  $\text{In}_2\text{Se}_3$  and  $\text{In}_2\text{S}_3$ ) [1–4], field-effect transistor [5,6], phase-changed memory [7,8], logic device [9], photoconductivity device [10,11], and lithium ion batteries [12]. Owing to the mismatch of valence electron numbers (e.g. (Ga, In)<sup>III</sup> and (S, Se)<sup>VI</sup>), the group III–VI compounds often show a variety of valency-changed structures with different stoichiometry and crystalline phases. The general-found stoichiometries for the III–VI chalcogenides are  $\text{MX}$  (M = Ga, In and X = S, Se) such as  $\text{InSe}$  [13],  $\text{M}_6\text{X}_7$  as  $\text{In}_6\text{S}_7$  [14] and  $\text{In}_6\text{Se}_7$  [15], and  $\text{M}_2\text{X}_3$  as  $\text{Ga}_2\text{S}_3$  [16] and  $\text{In}_2\text{Se}_3$  [7]. The

chalcogenides possess diversified crystal structure, dissimilar band diagram, different band gap and various chemical and physical properties. Among these chalcogenides, the sulfide compounds are non-toxic and more environmental friendly to be free of selenium. The III–VI sulfides may have interesting chemical and physical properties, however, to date, the lack of large and high quality crystals may become the main cause in evaluation (application) of the III–VI sulfide compounds [i.e. most of the reported results were done on physically or chemically deposited thin films with different crystalline state (amorphous or polycrystalline)] [3,17–19].

In this paper, high-quality crystals of  $\text{In}_2\text{S}_3$  and  $\text{Ga}_2\text{S}_3$  have been successfully grown by chemical vapor transport (CVT) method using  $\text{ICl}_3$  as the transport agent. The as-grown crystals show many relevant crystal faces and larger crystallite size. We present detailed characterization in near band edge, crystallinity, and interface states of the as-grown  $\text{In}_2\text{S}_3$  and  $\text{Ga}_2\text{S}_3$  crystals using thermoreflectance (TR), Raman, photoluminescence (PL), optical-absorption, and photo voltage-current (Photo V–I) measurements. The as-grown  $\text{In}_2\text{S}_3$  crystal essentially displays dark red and  $\text{Ga}_2\text{S}_3$  crystal reveals transparent and light-yellow colored. X-ray diffraction pattern confirms a tetragonal  $\beta$ -phase constructed in the as-grown

\* Corresponding author at: Graduate Institute of Applied Science and Technology, National Taiwan University of Science and Technology, Taipei 106, Taiwan.

E-mail address: [chho@mail.ntust.edu.tw](mailto:chho@mail.ntust.edu.tw) (C.-H. Ho).

$\text{In}_2\text{S}_3$  crystals while  $\text{Ga}_2\text{S}_3$  belongs to the monoclinic structure. For  $\text{In}_2\text{S}_3$ , the band gap of  $\beta\text{-In}_2\text{S}_3$  is about 1.935 eV at 300 K by TR and transmittance measurements. Because the existence of S vacancies and In interstitials, the  $\beta\text{-In}_2\text{S}_3$  crystal can form easily the surface oxidation states of  $\beta\text{-In}_2\text{S}_{3-3x}\text{O}_{3x}$  on its surface [17]. PL experiments reveal that the surface oxidation states formed by  $\beta\text{-In}_2\text{S}_{3-3x}\text{O}_{3x}$  are a series of higher-energy levels with transition energies higher above band gap of the  $\beta\text{-In}_2\text{S}_3$ . The energy distribution of the  $\beta\text{-In}_2\text{S}_{3-3x}\text{O}_{3x}$  oxide states is from 1.935 eV in  $\text{In}_2\text{S}_3$  to that of exceeding 3 eV in  $\text{In}_2\text{O}_3$ . The oxygen sensing behavior by  $\text{In}_2\text{S}_3$  with the formation of surface oxide (detected by PL) has been demonstrated and analyzed herein. The oxygen sensing is different from other resistive-type  $\text{O}_2$  sensor with sensing the resistance change by oxygen [20]. Besides, for  $\text{Ga}_2\text{S}_3$ , the TR spectra display three band-edge transitions denoted as  $E_A$ ,  $E_B$  and  $E_C$  detected at 300 K. The TR features of  $E_A = 3.052$  eV (direct gap) and  $E_B = 3.240$  eV can also be detected in the transmittance spectrum of  $\text{Ga}_2\text{S}_3$  at room temperature. The  $E_C$  feature of TR is a higher-energy transition of the monoclinic  $\text{Ga}_2\text{S}_3$ . The low-temperature PL spectrum of  $\text{Ga}_2\text{S}_3$  at 15 K demonstrates a white-light emission consisted of band-edge (BE) and defect ( $E_{d1}$  and  $E_{d2}$ ) luminescence. Photo V–I measurements of the  $\text{Ga}_2\text{S}_3$  sample under different illumination conditions of dark, halogen lamp, and 405 nm laser reveal that the  $\text{Ga}_2\text{S}_3$  is a highly-sensitive photoconductive material available for blue to ultraviolet (UV) photodetection. The  $\text{Ga}_2\text{S}_3$  photodetector usually possesses a lower band gap (3.052 eV) which can enhance blue to violet response with respect to that of the other ZnO UV detector of band gap  $\sim 3.4$  eV [21]. According to the experimental analysis, material properties and potential applications of the  $\text{M}_2\text{S}_3$  ( $\text{M} = \text{In, Ga}$ ) defect crystals are thus realized.

## 2. Experimental

### 2.1. Crystal growth

The  $\text{M}_2\text{S}_3$  ( $\text{M} = \text{In, Ga}$ ) crystals were grown by the CVT method using  $\text{ICl}_3$  as a transport agent [22]. The growth was conducted in a horizontal three-zone tube furnace. The temperature gradient was setting as  $680^\circ\text{C} \leftarrow 820^\circ\text{C} \rightarrow 680^\circ\text{C}$  for growing  $\text{In}_2\text{S}_3$  and arranging as  $850^\circ\text{C} \leftarrow 920^\circ\text{C} \rightarrow 850^\circ\text{C}$  for growing  $\text{Ga}_2\text{S}_3$  in sealed quartz ampoules (i.e. 2.2 cm OD, 1.9 cm ID, and 20 cm in length). The temperature gradient was  $-7^\circ\text{C}/\text{cm}$  for growing  $\text{In}_2\text{S}_3$  and  $-3.5^\circ\text{C}/\text{cm}$  for growing  $\text{Ga}_2\text{S}_3$ , respectively. Prior to the crystal growth, the pure elements of In, Ga, and S with proper stoichiometry together with a small amount of transport agent ( $\text{ICl}_3$ ) were put into the quartz ampoule, which was then cooled using liquid nitrogen, evacuated to approximately  $10^{-6}$  Torr, and then sealed by acetylene and oxygen torch. The mixture in the quartz tube was slowly heated to the growth temperatures to avoid any explosion. The reaction was maintained for 240 h for growing large single crystals. After the growth process, the as-grown crystals exhibited two distinct color groups: dark red color for  $\text{In}_2\text{S}_3$  and light yellow and transparent for  $\text{Ga}_2\text{S}_3$ .

### 2.2. Characterization

For X-ray measurements, several small crystals from each compound of the  $\text{M}_2\text{S}_3$  ( $\text{M} = \text{In, Ga}$ ) were finely ground and the X-ray powder patterns were taken and recorded by means of a slow moving radiation detector. The copper  $\text{K}\alpha$  radiation ( $\lambda = 1.542 \text{ \AA}$ ) was employed in the X-ray diffraction measurements and a silicon standard was used for experimental calibration. The structure and lattice constant of the  $\text{M}_2\text{S}_3$  compounds were respectively analyzed and determined.

TR experiments were carried out in a wider energy range of 1.25 to 3.6 eV. For the measurement of low-energy portion ( $E < 2$  eV), a 150 W tungsten halogen lamp filtered by a PTI 0.2 m monochromator provided the monochromatic light. A HUV2000B silicon photodiode was used for the optical detection. For  $E \geq 2$  eV, a 150 W xenon-arc lamp acted as the light source. The reflected light of the sample was detected by a photomultiplier tube and signal was recorded via an EG&G model 7265 dual phase lock-in amplifier. For thermal perturbation of sample, a quartz plate acted as the heat sink. The quartz plate was coated with a winding path of golden tracks for the heating element. The shape of the golden path was formed by a copper mask [23]. The heating path consists of two wide tracks at the end sections and one narrow track lying in between them. The narrow track in the middle section is designed to act as a heat generation source when electrical current passes through the heater. The function of the wide track at the end sections is to speed up the heat dissipation when electrical power is off. Each thin sample of the  $\text{M}_2\text{S}_3$  with relevant as-grown face was closely attached on the narrow track of the Au path by silicone grease. The on-off heating disturbance uniformly modulates the  $\text{M}_2\text{S}_3$  samples. PL experiments were carried out using a QE65000 spectrometer. The CCD array detections were employed in the PL measurements. The pumping light source was a helium-cadmium laser ( $\lambda = 325$  nm) or a Q-switched diode-pumped solid-state laser ( $\lambda = 266$  nm). A set of neutral density filters was used to change and control the pumping power of the laser. A RMC model 22 closed-cycle cryogenic refrigerator equipped with a model 4075 digital thermometer controller facilitates the implementation of temperature-dependent measurements. For Raman measurement, a Renishaw micro-Raman spectrometer equipped with a 514-nm  $\text{Ar}^+$  ion laser was used for the structural characterization of the  $\text{M}_2\text{S}_3$  materials. The laser spot size (diameter) was reduced to  $\sim 5 \mu\text{m}$  and laser power was adjusted to  $\sim 2$  mW.

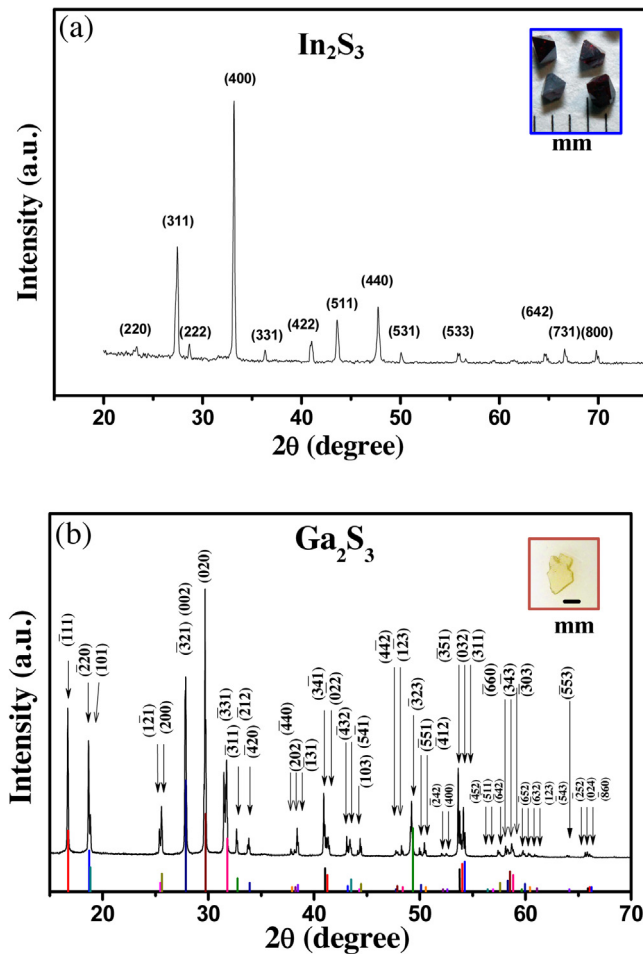
Photo V–I experiments were performed using two dissimilar light sources of tungsten halogen lamp and 405 nm laser as the solar emulators. The averaged power density was adjusted and maintained at approximate  $15 \text{ mW}/\text{cm}^2$  by using the monitor of an OPHIR optical power meter equipped with a broadband high-sensitivity thermal sensor ( $0.15\text{--}6 \mu\text{m}$ ). To prepare the sample for Photo V–I measurements, the specimen was cut into a rectangular shape with dimension of  $3.15 \times 2.95 \times 0.3 \text{ mm}^3$ . The two ends of each specimen were coated with Ag to act as the ohmic-contact electrodes. To perform the optical measurements, the ohmic-contact electrodes on each sample were shielded with light. The Photo V–I measurements were implemented using the auxiliary of a semiconductor parameter analyzer. The voltage scanning range of the apparatus was applied up to 1000 V ( $-1000$  V).

For oxidation and oxygen sensing test of  $\text{In}_2\text{S}_3$  with  $\text{O}_2$  pressure, the experiment was carried out in an evacuated horizontal quartz tube (i.e. diameter = 5 cm) in  $\text{O}_2$  ambient with flow rate control. The  $\text{O}_2$  partial pressure was respectively kept at 190, 380, 570, and 760 Torr to each of the surface-polished  $\text{In}_2\text{S}_3$  samples for 3-days oxidation. The temperature and relative humidity has been kept at  $T \sim 300$  K and  $\text{RH} \sim 0\%$ .

## 3. Results and discussion

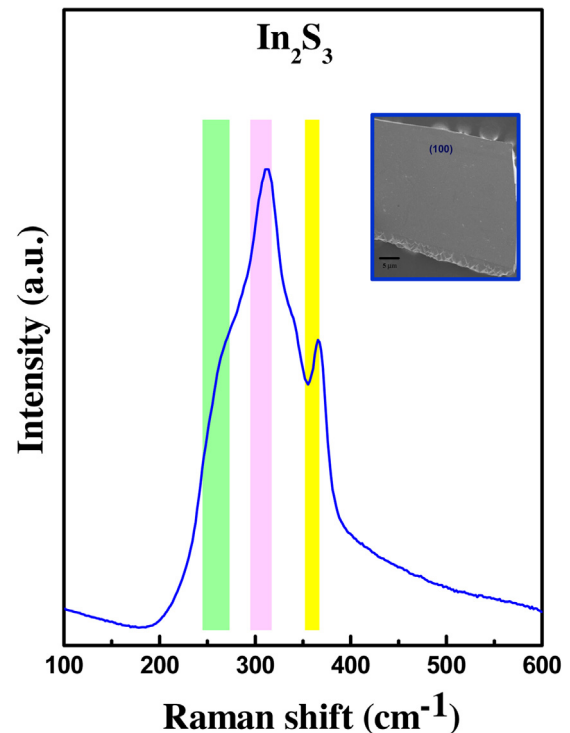
### 3.1. Crystal morphology and structure characterization

Fig. 1(a) shows the crystal morphology and X-ray diffraction (XRD) pattern of the as-grown  $\text{In}_2\text{S}_3$  crystals grown by CVT. The crystals reveal transparent and red colored. Most of them present a favorite crystalline face of  $\{100\}$ . From the formation of the outline shapes of the crystals, the crystallographic system tends to have a cubic ( $\alpha$ , Card No. 32-0456) or tetragonal ( $\beta$ , Card No. 25-0390)



**Fig. 1.** Powder X-ray diffraction patterns of the as-grown (a)  $\text{In}_2\text{S}_3$  and (b)  $\text{Ga}_2\text{S}_3$  crystals grown by CVT with  $\text{ICl}_3$  as the transport agent. The crystal morphology and crystal color of the  $\text{M}_2\text{S}_3$  ( $\text{M}=\text{In}, \text{Ga}$ ) crystals are also included in the insets for comparison. The results indicate  $\text{In}_2\text{S}_3$  belongs to tetragonal phase while  $\text{Ga}_2\text{S}_3$  is monoclinic structure.

crystalline phase. In general, the  $\beta$ -phase  $\text{In}_2\text{S}_3$  [24] possesses the same structure as that of  $\alpha$ - $\text{In}_2\text{S}_3$  except that the cation vacancies of  $\alpha$ - $\text{In}_2\text{S}_3$  are disordered in its lattice [25]. We index the XRD peaks in Fig. 1(a) as the  $\beta$ - $\text{In}_2\text{S}_3$ . The highest intensity of the (400) peak (i.e.  $2\theta=33.18^\circ$ ) reveals the preferred orientation in the tetragonal  $\beta$ - $\text{In}_2\text{S}_3$  crystals. It also verifies that the {100} plane is the most favorable as-grown surface of the tetragonal  $\beta$ - $\text{In}_2\text{S}_3$ . The lattice constants of the  $\beta$ - $\text{In}_2\text{S}_3$  were hence determined to be  $a=7.61 \text{ \AA}$ , and  $c=32.33 \text{ \AA}$  from XRD (i.e. comparing to  $a=7.619 \text{ \AA}$  and  $c=32.329 \text{ \AA}$  in Card No. 25-0390). The crystallography of  $\text{In}_2\text{S}_3$  is naturally a defect semiconductor possessing a spinel lattice with the cation vacancy randomly located on either octahedral site only or on both types of octahedral and tetrahedral sites [24]. The XRD result in Fig. 1(a) also indicates that the as-grown  $\beta$ - $\text{In}_2\text{S}_3$  may belong to a polycrystalline solid. Fig. 1(b) shows the XRD result of the as-grown  $\text{Ga}_2\text{S}_3$ . The crystal morphology and crystal color of the  $\text{Ga}_2\text{S}_3$  sample are also displayed in the inset of Fig. 1(b) for comparison. The  $\text{Ga}_2\text{S}_3$  crystal essentially shows transparent and yellow colored. The crystal color also implies that  $\text{Ga}_2\text{S}_3$  is a wide-band-gap semiconductor with its corresponding wavelength shorter than that of visible light. As shown in Fig. 1(b), many XRD peaks are observed in the angular range ( $2\theta$ ) between 10 and  $70^\circ$  owing to the lower symmetry of monoclinic structure comprised in the unit cell. The relative narrowed line-width broadening for each diffraction peak feature indicated that better quality of  $\text{Ga}_2\text{S}_3$  was existed in the as-



**Fig. 2.** Raman spectrum of the as-grown  $\text{In}_2\text{S}_3$  crystal on the {100} plane at room temperature. The result indicates  $\text{In}_2\text{S}_3$  is polycrystalline and belongs to  $\beta$  crystal phase [27].

grown crystals. The monoclinic symmetry of the as-grown  $\text{Ga}_2\text{S}_3$  is confirmed by comparing the data with previous XRD result of monoclinic  $\text{Ga}_2\text{S}_3$  (Card No. 48-1432 with showing color bars in Fig. 1(b), the lattice constants are  $a=11.09 \text{ \AA}$ ,  $b=9.578 \text{ \AA}$ ,  $c=6.395 \text{ \AA}$ , and  $\gamma=141.15^\circ$ ) [26]. The lattice constants for the monoclinic  $\text{Ga}_2\text{S}_3$  in Fig. 1(b) were determined to be  $a=11.11 \text{ \AA}$ ,  $b=9.58 \text{ \AA}$ ,  $c=6.4 \text{ \AA}$ , and  $\gamma=141.15^\circ$ , respectively.

Raman scattering spectroscopy can provide information about the vibration modes characteristic in crystal phase and crystalline states of the probed crystals. The vibration frequencies and line widths of the Raman modes are affected by local atomic arrangement including relative atomic oscillation, defects and structural disorder. Fig. 2 shows the Raman modes of the  $\text{In}_2\text{S}_3$  crystal on the {100} plane in the energy range between 100 and  $600 \text{ cm}^{-1}$ . The crystal morphology of the as-grown  $\text{In}_2\text{S}_3$  crystal on the {100} plane is also displayed in the inset of Fig. 2. The Raman spectrum in Fig. 2 exhibits approximate three broadened peak features of the vibration modes (not showing sharp and very narrow) which are caused by the as-grown  $\text{In}_2\text{S}_3$  typically being in a medium-range order and defect-like state. As shown in Fig. 2, the higher-energy Raman peak at  $366 \text{ cm}^{-1}$  can be ascribed to the  $\text{A}_{1g}$  mode [27] in the  $\beta$ - $\text{In}_2\text{S}_3$ . The strongest peak at  $\sim 312 \text{ cm}^{-1}$  is proposed to correlate with the symmetric stretching vibrating mode of  $\text{InS}_4$  tetrahedra [27] in the  $\text{In}_2\text{S}_3$  and the peak at  $\sim 258 \text{ cm}^{-1}$  may belong to the  $\text{E}_g$  mode [27]. The Raman result in Fig. 2 approximately verifies that the as-grown  $\text{In}_2\text{S}_3$  are  $\beta$  phase crystals, which exhibit a little bit amorphous and defect-contained state. Owing to the defect nature of  $\beta$ - $\text{In}_2\text{S}_3$ , we will evaluate and demonstrate the oxygen sensing ability and surface-oxide formation property of the crystal later.

Fig. 3(a) shows the Raman spectrum of  $\text{Ga}_2\text{S}_3$  in the energy range of  $200\text{--}500 \text{ cm}^{-1}$ . There are seven peak features at 234, 282, 309, 331, 348, 387, and  $427 \text{ cm}^{-1}$  detected in the  $\text{Ga}_2\text{S}_3$  crystal. Most of the frequencies can be assigned in terms of internal and external vibrations of tetrahedral  $\text{GaS}_4$  groups [28,29]. The symmetric  $\text{GaS}_4$  molecule has four fundamental vibration modes expressed by

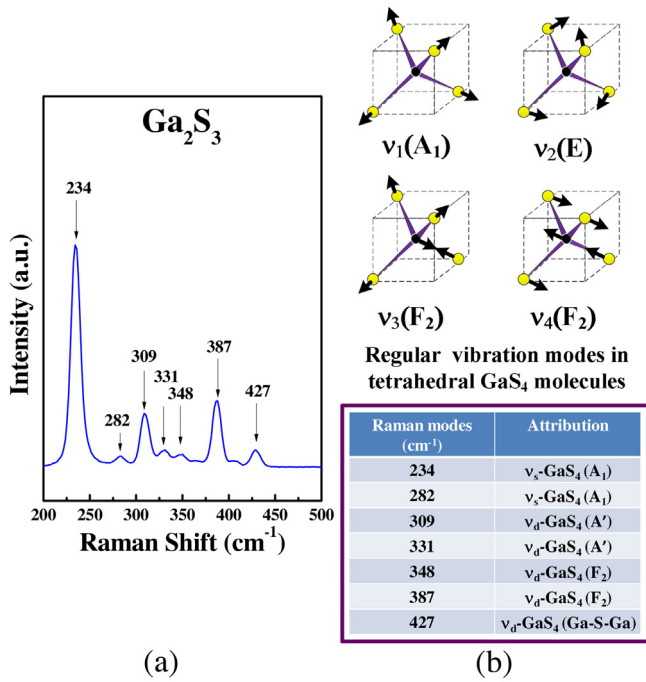


**Fig. 3.** (a) The Raman spectrum of monoclinic  $\text{Ga}_2\text{S}_3$  crystal done on the  $c$  plane. (b) Representative schemes of the normal vibration modes of  $\nu_1(A_1)$ ,  $\nu_2(E)$ ,  $\nu_3(F_2)$ , and  $\nu_4(F_2)$  in the  $\text{GaS}_4$  tetrahedra molecular unit inside the digallium trisulfide. The lower part shows the assignments of vibration frequencies [29] that detected in (a).

$\Gamma = A_1 + E + F_1 + F_2$  [29] as indicated in the upper part in Fig. 3(b). For the Raman scattering of the monoclinic  $\text{Ga}_2\text{S}_3$ , the dominant peaks are located at 234 and 387  $\text{cm}^{-1}$  (see Fig. 3(a)), which can be primarily associated with the  $\nu_1(A_1)$  and  $\nu_4(F_2)$  modes [29] of the  $\text{GaS}_4$  molecular unit. The lower part of Fig. 3(b) shows the assignments of the Raman modes observed in Fig. 3(a), and their association with vibrations of the  $\text{GaS}_4$  molecules in the upper part in Fig. 3(b). The structure of monoclinic  $\text{Ga}_2\text{S}_3$  is close to a defective wurtzite structure (like  $\gamma\text{-In}_2\text{Se}_3$  [30]) and which exhibits tetrahedral bonding with one-third Ga sites (on the average) are vacant tend to broaden the line widths of the Raman peak features. The Raman peak features in Fig. 3(a) reveal relative narrowed line widths and more peak modes as comparing to those of the  $\text{In}_2\text{S}_3$  in Fig. 2. It indicates that the as-grown  $\text{Ga}_2\text{S}_3$  crystals possess higher quality and crystallize in the monoclinic structural phase with lower symmetry as comparing to that of the tetragonal (cubic-like)  $\beta\text{-In}_2\text{S}_3$ .

### 3.2. Near-band-edge optical property

Fig. 4(a) shows the transmittance spectrum of  $\beta\text{-In}_2\text{S}_3$  at 300 K together with the corresponding TR spectrum is also included for comparison. The dashed line in Fig. 4(a) is the experimental TR data and the open-circle line is the least-square fit to a first derivative Lorentzian line-shape function expressed as [31]:

$$\frac{\Delta R}{R} = \text{Re} \left[ \sum A e^{j\phi} (E - E_0 + j\Gamma)^{-2} \right], \quad (1)$$

where  $A$  and  $\phi$  are the amplitude and phase of the line shape, and  $E_0$  and  $\Gamma$  are the energy and broadening parameter of the interband transition of  $\beta\text{-In}_2\text{S}_3$ . The obtained transition energy of  $\beta\text{-In}_2\text{S}_3$  from the fit is  $E_0 = 1.935 \text{ eV}$  at 300 K. The energy value matches well with the center position of the absorption edge of the corresponding transmittance spectrum in Fig. 4(a). The mathematical derivative spectrum of the transmittance data is also shown in Fig. 4(a) for comparison. The spectral line shape and center loca-

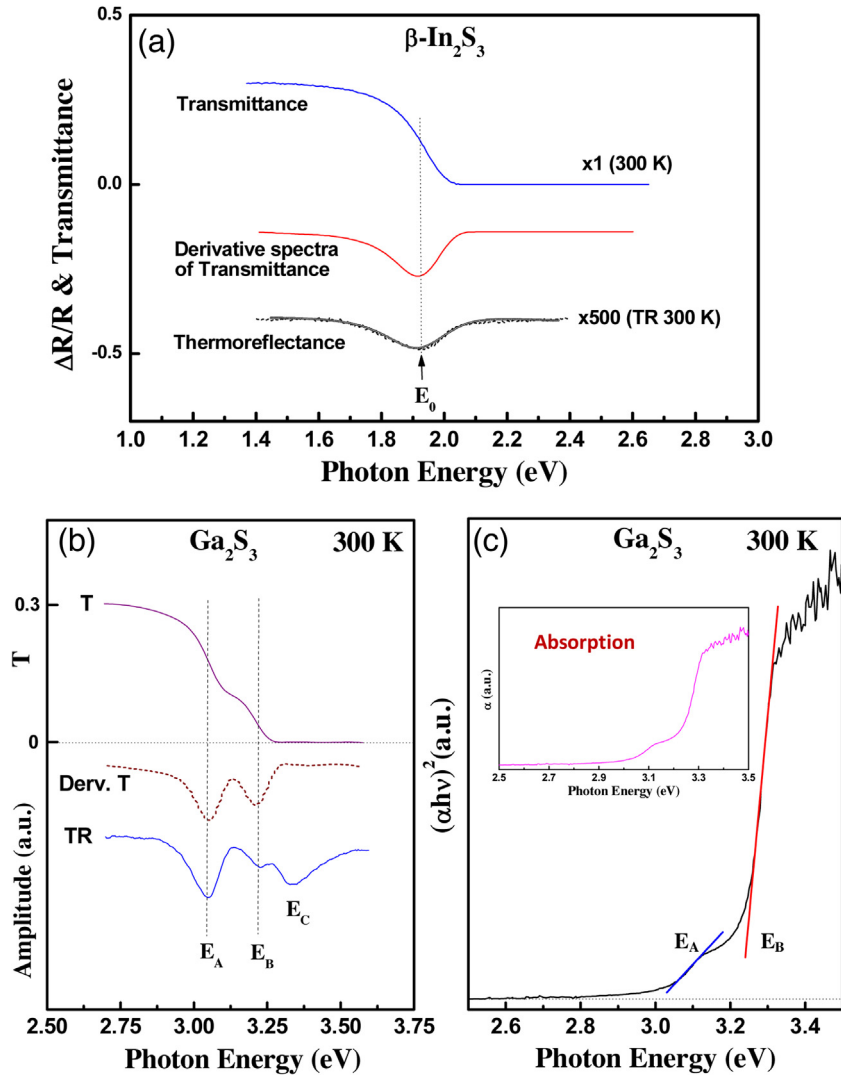
tion are nearly in accordance with those of the TR spectrum in Fig. 4(a). All the evidences in Fig. 4(a) reveal that the  $\beta\text{-In}_2\text{S}_3$  is a direct semiconductor with a direct band gap of  $\sim 1.935 \text{ eV}$ .

Fig. 4(b) shows the transmittance spectrum of the  $\text{Ga}_2\text{S}_3$  sample with energy range close to the band-edge portion. For comparison purpose the derivative T spectrum (Deriv. T) is also calculated, together with the TR spectrum of the  $\text{Ga}_2\text{S}_3$  is included in Fig. 4(b) for comparison. The absorption edge in the T spectrum of Fig. 4(b) shows two stair steps positioned between 2.8 and 3.4 eV at 300 K. It shows that the  $E_A$  and  $E_B$  transitions in TR are matching well with the Deriv. T spectrum calculated from T (i.e. TR is also derivative line shape) associated with the two stair steps. The result suggests that  $E_A$  and  $E_B$  are two of the direct band-edge transitions in  $\text{Ga}_2\text{S}_3$ . The calculated absorption coefficient  $\alpha$  in the inset of Fig. 4(c) also sustains that the spectral analysis of both  $E_A$  and  $E_B$  followed  $\alpha \propto (E - E_i)^{1/2}$ , a direct allowed transition ( $i = A$  or  $B$ ). The converted spectrum of  $(\alpha h\nu)^2$  versus  $h\nu$  plot shown in Fig. 4(c) also demonstrates that the linear fitting results get energy values of  $E_A = 3.052 \text{ eV}$  and  $E_B = 3.24 \text{ eV}$  for the monoclinic  $\text{Ga}_2\text{S}_3$ . This result sustains that  $\text{Ga}_2\text{S}_3$  is a direct semiconductor with a direct band gap positioned at  $E_A \approx 3.052 \text{ eV}$  at room temperature. The  $E_B$  and  $E_C$  features shown in the TR spectrum of Fig. 4(b) are higher-energy transitions above band edge. Previous polarization-dependent TR measurements (done on the  $c$  plane) of  $\text{Ga}_2\text{S}_3$  revealed that the  $E_B$  transition is present only in the  $E \parallel a$ -axis polarization while the  $E_C$  excitons are merely allowed at the  $E \perp a$ -axis polarization [32]. The  $E_B$  and  $E_C$  are coming from different origins. The highest valence band of the monoclinic  $\text{Ga}_2\text{S}_3$  may consist of mainly S-3p and some Ga-4p orbitals [33]. Unlike the other s orbital has highly spherical symmetry, the p states in the valence band of  $\text{Ga}_2\text{S}_3$  are strongly oriented dumb-bell shape (axial dependent) distribution, which may enhance the anisotropic character present in the optical property of the  $\text{Ga}_2\text{S}_3$ . For the lowest conduction-band portion of  $\text{Ga}_2\text{S}_3$ , the density of state is mainly composed of Ga-4s and a little S-3p states.

### 3.3. Oxygen sensing behavior and surface oxide formation on $\beta\text{-In}_2\text{S}_3$

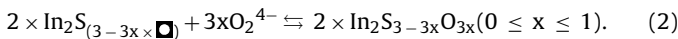
The III–VI  $\beta\text{-In}_2\text{S}_3$  is a defect-type semiconductor that comprising of many sulfur vacancies  $V_S$  (donor), indium vacancies  $V_{In}$  (acceptor), and indium interstitials  $I_{In}$  (donor) in the unit cell. Because the existence of S vacancies and In interstitials, the  $\beta\text{-In}_2\text{S}_3$  crystal can form easily the surface oxidation states of  $\beta\text{-In}_2\text{S}_{3-3x}\text{O}_{3x}$  [17] in ambient air (or  $\text{O}_2$ ) by chemical reaction of In–O. The surface oxidation behavior provides a promising application of  $\beta\text{-In}_2\text{S}_3$  for oxygen sensing and ultraviolet optical absorption. Fig. 5(a) shows the PL spectra of a  $\beta\text{-In}_2\text{S}_3$  crystal after the oxidation time of 1, 3, and 10 days in atmosphere with a relative humidity RH  $\sim 50\text{--}60\%$  (i.e. the obtained crystals were broken from an evacuated quartz tube). Three main peaks of PL emission can be detected in the PL spectrum of  $\beta\text{-In}_2\text{S}_3$  in Fig. 5(a) after 3 days oxidation (yellow-circle line). The  $P_1$  peak below 2 eV may come from the band-edge emission of the  $\text{In}_2\text{S}_3$  part, while the  $P_3$  peak at  $\sim 3.26 \text{ eV}$  is the excitonic emission of  $\text{In}_2\text{O}_3$  [34]. The broadened  $P_2$  peak of  $\sim 2.55 \text{ eV}$  that lies in between the energies of  $P_1$  and  $P_3$  can be assigned as the PL emission from the surface oxidation part of the  $\beta\text{-In}_2\text{S}_{3-3x}\text{O}_{3x}$  ( $0 < x < 1$ ). As shown in Fig. 5(a), for the  $\text{In}_2\text{O}_3$  ( $P_3$ ) peak, the PL intensity of the sample after 1 day oxidation shows much lower than those of the other 3 days and 10 days oxidations. The PL intensity of the  $P_3$  ( $\text{In}_2\text{O}_3$ ) peak after 10 days oxidation even display very prominent strength with respect to those of the other 1-day and 3-days oxidation samples. However, for the  $P_1$  peak coming from the  $\text{In}_2\text{S}_3$ , the relative low PL intensity after 10 days oxidation in Fig. 5(a) may be attributed to the increase of indium-oxide ( $\text{In}_2\text{O}_3$ ) thickness deposited on the surface of the  $\beta\text{-In}_2\text{S}_3$ , which can lower down the PL signal of the  $\text{In}_2\text{S}_3$  part such as the indication scheme





**Fig. 4.** (a) Transmittance and TR spectra of  $\beta\text{-In}_2\text{S}_3$  in the energy range of 1.4–2.6 eV at 300 K. (b) Spectral comparison of T, Derv. T, and TR measurements of the  $\text{Ga}_2\text{S}_3$  crystal at room temperature. (c) The absorption spectrum and the result of  $(\alpha h\nu)^2$  vs.  $h\nu$  for the determination of transition energies of  $E_A$  and  $E_B$ .

shown in the middle inset of Fig. 5(b). When the as-grown  $\text{In}_2\text{S}_3$  was put in air, the surface sulfur vacancies  $V_S$  may have the possibility to react with ambient oxygen, especially on the surface. This is a gas sensing behavior of oxygen for  $\beta\text{-In}_2\text{S}_3$ . The first is adsorption with  $\text{O}_2$  on its surface. The interaction with atmosphere oxygen can produce ionosorption of molecular  $\text{O}_2^{4-}$  and atomic ( $\text{O}^{2-}$ ,  $\text{O}_2$ ) species at room temperature. The charge transfer and chemical reaction between the occupants  $\text{O}_2^{4-}$  (stay in the S–S vacancies) and the cation  $\text{In}^{3+}$  ions by taking into account the stoichiometric change from inner layer to the outmost layer can be [35]:



Where the oxygen content is changed from  $x=0$  (the inner part  $\sim\text{In}_2\text{S}_3$ ) to  $x=1$  (the outmost part  $\sim\text{In}_2\text{O}_3$ ), and “ $\blacksquare$ ” is the sulfur vacancy in the unit cell of  $\beta\text{-In}_2\text{S}_3$ . For the oxygen sensing, the integrated strength of the PL intensity of the  $\text{P}_3$  ( $\text{In}_2\text{O}_3$ ) peak [in Fig. 5(a)] can be further analyzed to obtain the sensing index of the ambient oxygen and we will analyze and discuss the relationship later. To verify the surface oxidation behavior of  $\text{In}_2\text{S}_3$ , the PL spectra of a surface-polished and an unpolished (1 day oxidation) sample are respectively shown in Fig. 5(b) for comparison. For the surface-polished sample in Fig. 5(b), the  $\text{P}_2$  peak [i.e. caused

by the  $\text{In}_2\text{S}_{3-3x}\text{O}_{3x}$  ( $0 < x < 1$ )] shows decrease. However, the band-edge emission of  $E_0$  (at  $\sim 1.935$  eV) and defect luminescence of  $E_d$  from the intrinsic defects (i.e.  $V_S$  donor  $\rightarrow V_{\text{In}}$  acceptor at  $\sim 1.5$  eV) are simultaneously enhanced. It reveals that the removal of the surface oxide by the polishing of the  $\beta\text{-In}_2\text{S}_3$  sample can enhance the intrinsic defect and band-edge emissions of  $\text{In}_2\text{S}_3$ . The band-edge scheme for the origins of the  $E_d$  and  $E_0$  luminescence is also included in the lower inset of Fig. 5(b) for comparison.

The oxygen sensing behavior by the formation of surface indium oxide on  $\beta\text{-In}_2\text{S}_3$  has been evident in Fig. 5(a) and (b). When the as-grown  $\beta\text{-In}_2\text{S}_3$  crystal was broken from the evacuated quartz tube and put in atmosphere for one day, the surface oxide was gradually formed with the inner content of  $\text{In}_2\text{S}_{3-3x}\text{O}_{3x}$  ( $0 < x < 1$ ) but the outer layer of  $\text{In}_2\text{O}_3$ . The oxygen content and sensing index by  $\text{In}_2\text{S}_3$  (in air) was achieved by measuring the PL intensity coming from the well-formed  $\text{In}_2\text{O}_3$  [ $\text{P}_3$  in Fig. 5(a)] outmost layer. Previous secondary ion mass spectroscopy (SIMS) result had showed that the thickness of the  $\text{In}_2\text{O}_3$  outmost layer is about 100 nm for one day oxidation in atmosphere (i.e. not showing here). The dependence of thickness vs. time for the  $\text{In}_2\text{O}_3$  is shown in the inset of Fig. 6(a). It is approximate a linear relation with a growth rate of  $\sim 100$  nm/day for  $\text{In}_2\text{O}_3$  on  $\text{In}_2\text{S}_3$ . The growth rate of oxide is slightly lower than that of  $\alpha\text{-In}_2\text{Se}_3$  [i.e.  $\text{In}_2\text{O}_3$  on  $\alpha\text{-In}_2\text{Se}_3$  is  $\sim 250$  nm/day] owing to

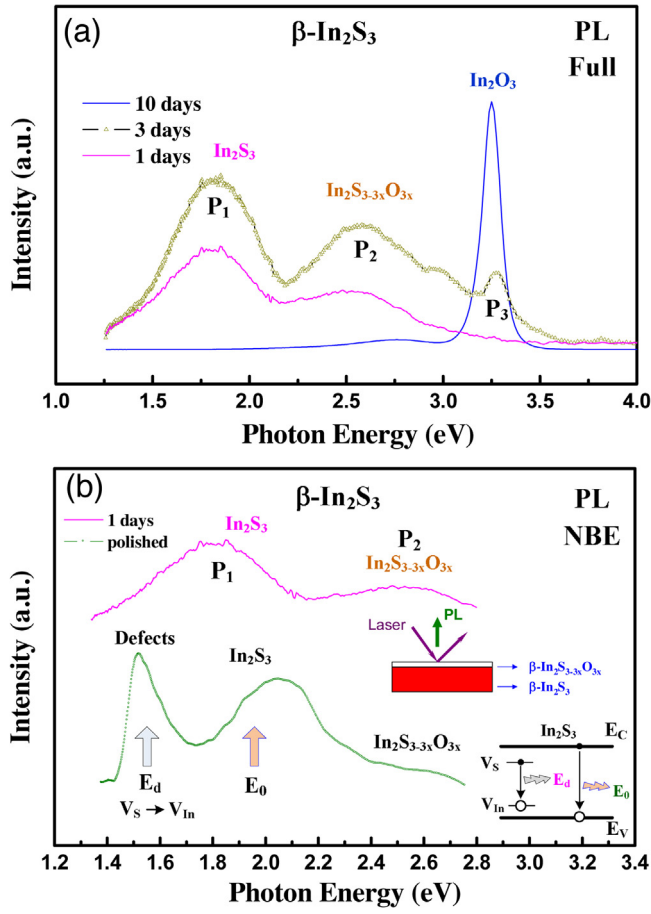


**Fig. 5.** (a) Full-range PL spectra of  $\beta$ - $\text{In}_2\text{S}_3$  after the oxidation in ambient air of 1, 3, and 10 days between 1.25 and 4 eV. (b) Spectral comparison of a surface polished and an unpolished (1 day oxidation)  $\text{In}_2\text{S}_3$  sample near band edge. The insets respectively depict the surface-oxidation and band-edge scheme of the  $\text{In}_2\text{S}_3$  crystal.

the 2D-like layered  $\alpha$ - $\text{In}_2\text{Se}_3$  have effectively a large sheet area [35]. Besides, the oxide layer thickness of  $\text{In}_2\text{O}_3$  was also measured under different  $\text{O}_2$  partial pressure of 0–760 Torr that forms on  $\text{In}_2\text{S}_3$ . The relation of thickness versus  $\text{O}_2$  pressure also demonstrated, approximately, a linear change similar to that of the thickness versus oxidation time. For the PL detection of  $\text{In}_2\text{O}_3$ , Fig. 6(a) displays the relative PL intensity ratio (PLR) as a function of reaction time when the as-grown  $\text{In}_2\text{S}_3$  crystal was put in atmosphere from one to ten days (i.e. at room temperature and  $\text{RH} \approx 50$ –60%). The PLR is defined as intensity ratio of  $I_{P3}(E=3.26 \text{ eV})/I_{E=4.0 \text{ eV}}$  [see Fig. 5(a)] of the  $\text{In}_2\text{O}_3$  emission. The relationship demonstrates an exponential-like variation for the intensity change of oxidation time. The blue line in Fig. 6(a) shows the fitting result of the experimental data fitted to an exponential formula expressed as  $I(t)=I_0 \cdot t^a$ , where  $I_0$  is the PLR value of the  $\text{In}_2\text{O}_3$  after 1 day oxidation,  $t$  is oxidation time, and  $a$  is the exponential-term parameter. The obtained fitting parameters are  $I_0 = 1.8 \pm 0.2$  and  $a = 2.56 \pm 0.03$ , respectively. From the obtained formula of PLR by PL, the long-term ambient oxygen (e.g.  $\sim 21\%$   $\text{O}_2$  content in air) sensing by  $\text{In}_2\text{S}_3$  has been realized. Fig. 6(b) displays the relation of PLR versus  $\text{O}_2$  partial pressure (190, 380, 570, and 760 Torr) that detected in a surface-polished  $\text{In}_2\text{S}_3$  sample for 3 days oxidation. The open circles are the experimental PLR values and the solid line is the least-square fit of experimental data to an exponential expression as  $I(p)=I_{p0} \cdot p^b$ , where  $p$  is the oxygen pressure (in Torr) and  $b$  is the exponential-term parameter. The obtained fitting parameters from the fit in Fig. 6(b) are  $I_{p0} = (8 \pm 4) \times 10^{-5}$  and  $b = 2.54 \pm 0.06$ , respectively. The obtained

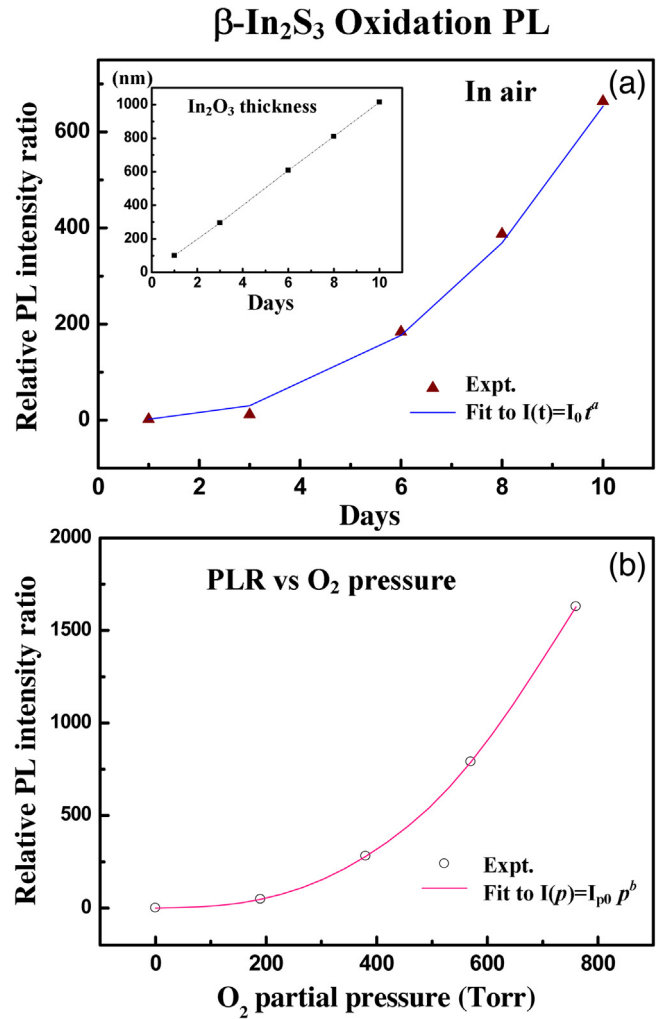


**Fig. 6.** (a) The relative PL intensity ratio (PLR) versus oxidation time for the formation of  $\text{In}_2\text{O}_3$  layer on  $\text{In}_2\text{S}_3$  under atmosphere. The inset shows the grown thickness of  $\text{In}_2\text{O}_3$  with different growth time on the  $\text{In}_2\text{S}_3$ . (b) The dependence of PLR versus  $\text{O}_2$  pressure for a polished  $\text{In}_2\text{S}_3$  crystal (i.e. oxidation for three days).

relation of  $I(p)$  can be the sensing index of different  $\text{O}_2$  pressure ambient, that got from a polished  $\beta$ - $\text{In}_2\text{S}_3$  crystal.

### 3.4. Luminescence and UV optical property of $\text{Ga}_2\text{S}_3$

Displayed in the left part of Fig. 7(a) is the low-temperature and wider-range PL spectrum of the  $c$ -plane  $\text{Ga}_2\text{S}_3$  at 15 K. The excitation source is a 325 nm He-Cd laser. There are three main bands of emission denoted as  $E_{d1}$ ,  $E_{d2}$ , and BE could be detected in the PL measurement. The  $E_{d1}$  ( $\sim 1.99 \text{ eV}$ ) and  $E_{d2}$  ( $\sim 2.79 \text{ eV}$ ) bands are the defect related luminescence originated from the donors and acceptors in the  $\text{Ga}_2\text{S}_3$  crystals while the BE band ( $\sim 3.36 \text{ eV}$ ) must be the band-edge emission [32]. The representative band scheme of the  $E_{d1}$ ,  $E_{d2}$ , and BE emissions in  $\text{Ga}_2\text{S}_3$  is depicted in the inset of left Fig. 7(a) for comparison. The  $E_{d1}$  is originated from the sulfur vacancies (donor band) to the upper acceptor level and  $E_{d2}$  may come from the donor band to the lower acceptor level. The assignments of the  $E_{d1}$  and  $E_{d2}$  emissions are based on the temperature-dependent PL spectra of  $\text{Ga}_2\text{S}_3$  from 15 to 300 K (3D plot) shown in the right side of Fig. 7(a). The relative intensity change of  $E_{d1}$  and  $E_{d2}$  with temperature increasing shows the  $E_{d1}$  peak decreased while the  $E_{d2}$  peak was increased from 15 to 300 K. It is attributed to the temperature ionization of electrons between the  $E_{d1}$  and  $E_{d2}$  acceptor levels as shown in the inset of the left-side Fig. 7(a). The acceptor levels

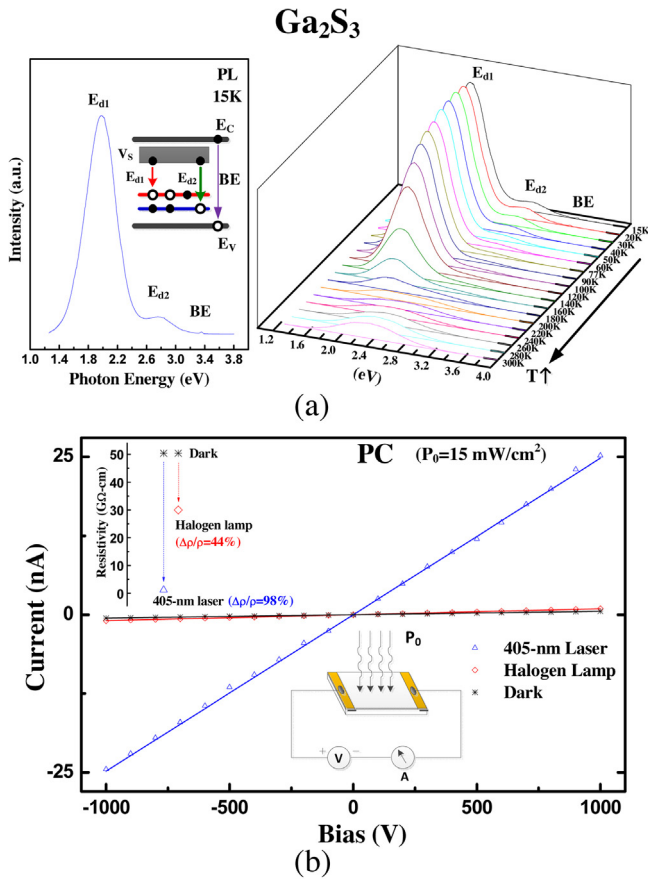


**Fig. 7.** (a) Low-temperature and wide-range PL spectrum of monoclinic Ga<sub>2</sub>S<sub>3</sub> on the c plane at 15 K. The temperature-dependent PL spectra of Ga<sub>2</sub>S<sub>3</sub> in the temperature range between 15 and 300 K are also shown (3D plot). (b) Photo V-I measurement result at different illumination condition of dark, halogen lamp and 405 nm laser for a Ga<sub>2</sub>S<sub>3</sub> photoconductor. The photo-resistivity change and measurement setup respectively depict in the upper and lower insets. The 405 nm laser reveals higher photoresponsivity.

of E<sub>d1</sub> and E<sub>d2</sub> are maybe coming from the Ga vacancies (V<sub>Ga</sub>) of the Ga<sub>2</sub>S<sub>3</sub> defect-type semiconductor. As shown in the left part of Fig. 7(a), the appearance of the band-edge emission BE sustains a better crystalline quality of the as-grown Ga<sub>2</sub>S<sub>3</sub> crystal than those of the other polycrystalline and thin-film forms of the Ga<sub>2</sub>S<sub>3</sub> in the literatures [36,19].

In order to evaluate the UV photo-sensing behavior of the Ga<sub>2</sub>S<sub>3</sub> crystal, Photo V-I measurements are implemented at 300 K. Fig. 7(b) shows the Photo V-I measurement results of the Ga<sub>2</sub>S<sub>3</sub> crystal under different illumination conditions of dark, halogen lamp, and 405 nm laser. Essentially they are the photoconductivity (PC) results of Ga<sub>2</sub>S<sub>3</sub> under various light sources' illumination. The measurement setup is shown in the lower inset of Fig. 7(b). The illumination power density of all the light sources was kept at P<sub>0</sub> ≈ 15 mW/cm<sup>2</sup>. Nearly a linear relationship for the Photo V-I curves was obtained in Fig. 7(b) (i.e. by a linear fitting). The obtained values of resistivity are ρ = 53.4 GΩ-cm for the dark condition, ρ = 30 GΩ-cm for the halogen lamp, and ρ = 1.15 GΩ-cm for the 405 nm laser illumination, respectively. The resistivities under dark, halogen lamp, and 405 nm laser illumination are respectively depicted as star, hollow diamond, and open triangle in the upper inset of Fig. 7(b). The halogen lamp represents a broadband blackbody radiation with a main hump peak close to approximate 1.9 eV, which will gradually decrease its intensity toward to the UV region. The photoconduction ratio of the halogen lamp is about Δρ/ρ<sub>dark</sub> = 44%. For the 405 nm laser (with the same power density),

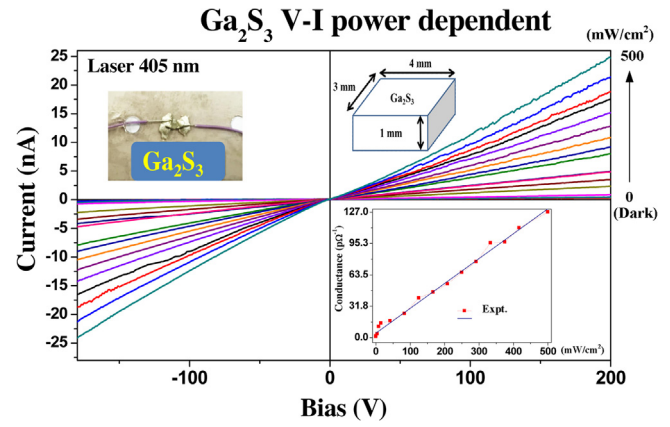


**Fig. 8.** Powder dependent Photo V-I measurements of a Ga<sub>2</sub>S<sub>3</sub> photoconductor illuminated by a 405 nm laser under different power density from 0 to 500 mW/cm<sup>2</sup>. The upper insets show the sample image (with Ag contacts) and sample size of the photoconductor. The lower inset depicts the dependency of conductance versus power densities of the shiny laser. They show a linear dependence with the laser power change.

the photoconduction ratio can reach Δρ/ρ<sub>dark</sub> = 98%. The photon energy of the 405 nm laser is 3.062 eV, which is larger than that of the direct band gap (E<sub>A</sub> ≈ 3.052 eV) of Ga<sub>2</sub>S<sub>3</sub> to render a significant photoresponse from blue to UV region such as the PC result shown in Fig. 7(b). To obtain a real UV sensing formula from the 405 nm laser, power dependent Photo V-I measurements (from 0 to 500 mW/cm<sup>2</sup>) using the Ga<sub>2</sub>S<sub>3</sub> crystal are implemented and the results are demonstrated in Fig. 8. The sample image and sample size of the Ga<sub>2</sub>S<sub>3</sub> photoconductor are shown in the insets in Fig. 8. With the incident power density of the 405 nm laser was increased, the V-I results of the Ga<sub>2</sub>S<sub>3</sub> photoconductor revealed increased photoconductance as shown in Fig. 8. The experimental data of the conductance (G) versus laser power density (P) are shown by solid squares in the lower inset of Fig. 8. It shows approximately a linear relation of G vs. P in Ga<sub>2</sub>S<sub>3</sub> by the illumination of a 405 nm laser. A linear fit of the experimental data (in the lower inset of Fig. 8) also reveals a relation of G(P) = G<sub>0</sub> + s·P can be obtained, where the values of G<sub>0</sub> = 4.6 × 10<sup>-12</sup> Ω<sup>-1</sup> and s = 2.52 × 10<sup>-13</sup> Ω<sup>-1</sup> cm<sup>2</sup>/mW are respectively obtained. It will be the sensing-index relation of the Ga<sub>2</sub>S<sub>3</sub> crystal illuminated by a 405 nm laser at different power densities.

#### 4. Conclusions

In conclusion, In<sub>2</sub>S<sub>3</sub> and Ga<sub>2</sub>S<sub>3</sub> crystals have been successfully grown by CVT method with ICl<sub>3</sub> as the transport agent. All the optical experiments indicate that the III-VI M<sub>2</sub>S<sub>3</sub> (M = In, Ga) crystals are defect-type semiconductors possessing many intrinsic defects such as V<sub>S</sub> and V<sub>In</sub> (or V<sub>Ga</sub>) inside the crystals for rendering a lot of defect emissions. Owing to the defect nature and misvalency of the III-VI compounds, the In<sub>2</sub>S<sub>3</sub> may crystallize in a tetragonal structure while the as-grown Ga<sub>2</sub>S<sub>3</sub> would belong to the monoclinic phase with lower symmetry. The band gaps of In<sub>2</sub>S<sub>3</sub> and Ga<sub>2</sub>S<sub>3</sub> are respectively determined to be 1.935 eV and 3.052 eV. They are all direct semiconductors. The In<sub>2</sub>S<sub>3</sub> defect semiconductor with sulfur vacancy has been proven to easily from surface oxide In<sub>2</sub>S<sub>3-3x</sub>O<sub>3x</sub> (0 ≤ x ≤ 1) by In-O reaction with its inner layer content approaching In<sub>2</sub>S<sub>3</sub> while the outmost composition close to In<sub>2</sub>O<sub>3</sub>. This property renders In<sub>2</sub>S<sub>3</sub> becoming an oxygen sensor by using PL intensity analysis as the detection index. Moreover, the characteristics of wider band gap and defect style render monoclinic Ga<sub>2</sub>S<sub>3</sub> being a white-light luminescence matter and a superior blue to UV photodetector material available for optoelectronics use. By the illumination of a 405 nm laser of different power density (from

0 to 500 mW/cm<sup>2</sup>), a sensing index of linear relationship of the conductance G versus power density P was obtained using the Ga<sub>2</sub>S<sub>3</sub> photoconductor.

## Acknowledgment

This work was financially supported by the Ministry of Science and Technology of Taiwan under the Grant No. MOST 104-2112-M-011-002-MY3.

## References

- [1] S.H. Kwon, B.T. Ahn, S.K. Kim, K.H. Yoon, J. Song, Growth of CuIn<sub>3</sub>Se<sub>5</sub> layer on CuInSe<sub>2</sub> films and its effect on the photovoltaic properties of In<sub>2</sub>Se<sub>3</sub>/CuInSe<sub>2</sub> solar cells, *Thin Solid Films* 323 (1998) 265–269.
- [2] H. Peng, D.T. Schoen, S. Meister, X.F. Zhang, Y. Cui, Synthesis and phase transformation of In<sub>2</sub>Se<sub>3</sub> and CuInSe<sub>2</sub> nanowires, *J. Am. Chem. Soc.* 129 (2007) 34–35.
- [3] T. Todorov, J. Carda, P. Escribano, A. Grimm, J. Klaer, R. Klenk, Electro deposited In<sub>2</sub>S<sub>3</sub> buffer layers for CuInS<sub>2</sub> solar cells, *Sol. Energy Mater. Sol. Cells* 92 (2008) 1274–1278.
- [4] J. Kim, H. Hiroi, T.K. Todorov, O. Gunawan, M. Kuwahara, T. Gokmen, D. Nair, M. Hopstaken, B. Shin, Y.S. Lee, W. Wang, H. Sugimoto, D.B. Mitzi, High efficiency Cu<sub>2</sub>ZnSn(S, Se)<sub>4</sub> solar cells by applying a double In<sub>2</sub>S<sub>3</sub>/CdS emitter, *Adv. Mater.* 26 (2014) 7427–7431.
- [5] T. Zhai, Y. Ma, L. Li, X. Fang, M. Liao, Y. Koide, J. Yao, Y. Bando, D. Golberg, Morphology-tunable In<sub>2</sub>Se<sub>3</sub> nanostructures with enhanced electrical and photoelectrical performances via sulfur doping, *J. Mater. Chem.* 20 (2012) 6630–6637.
- [6] B. Mitzi, M. Copel, S.J. Chey, Low-voltage transistor employing a high-mobility spin-coated chalcogenide semiconductor, *Adv. Mater.* 17 (2005) 1285–1289.
- [7] K. Lai, H. Peng, W. Kundhikanjana, D.T. Schoen, C. Xie, S. Meister, Y. Cui, M.A. Kelly, Z.X. Shen, Nanoscale electronic inhomogeneity in In<sub>2</sub>Se<sub>3</sub> nanoribbons revealed by microwave impedance microscopy, *Nano Lett.* 9 (2009) 1265–1269.
- [8] C.H. Ho, Amorphous effect on the advancing of wide-range absorption and structural-phase transition in  $\gamma$ -In<sub>2</sub>Se<sub>3</sub> polycrystalline layers, *Sci. Rep.* 4 (2014) 4764.
- [9] J.Y. Lee, K. Sun, B. Li, Y.H. Xie, X. Wei, T.P. Russell, Multi-level threshold switching behavior of In<sub>2</sub>Se<sub>3</sub> confined in nanostructured silicon substrate, *Appl. Phys. Lett.* 97 (2010) 092114.
- [10] R. Sreekumar, R. Jayakrishnan, S.K. Kartha, K.P. Vijayakumar, S.A. Khan, D.K. Avasthi, Enhancement of band gap and photoconductivity in gamma indium selenide due to swift heavy ion irradiation, *J. Appl. Phys.* 103 (2008) 023709.
- [11] C.H. Ho, Y.P. Wang, C.H. Chan, Y.S. Huang, C.H. Li, Temperature-dependent photoconductivity in  $\beta$ -In<sub>2</sub>S<sub>3</sub> single crystals, *J. Appl. Phys.* 108 (2010) 043518.
- [12] M.S. Whittingham, Chemistry of intercalation compounds: metal guests in chalcogenide hosts, *Prog. Solid State Chem.* 12 (1978) 41–99.
- [13] S.R. Tamalampudi, Y.Y. Lu, U.R. Kumar, R. Sankar, C.D. Liao, B.K. Moorthy, C.H. Cheng, F.C. Chou, Y.T. Chen, High performance and bendable few-layered InSe photodetectors with broad spectral response, *Nano Lett.* 14 (2014) 2800–2806.
- [14] C.H. Ho, Y.P. Wang, Y.S. Huang, Optical characterization of band-edge property of In<sub>6</sub>S<sub>7</sub> compound, *Appl. Phys. Lett.* 100 (2012) 131905.
- [15] J.H.C. Hogg, The crystal structure of In<sub>6</sub>Se<sub>7</sub>, *Acta Crystallogr. Sect. B* 27 (1971) 1630–1634.
- [16] J.S. Lee, Y.H. Won, H.N. Kim, C.D. Kim, W.T. Kim, Photoluminescence of Ga<sub>2</sub>S<sub>3</sub> and Ga<sub>2</sub>S<sub>3</sub>:Mn single crystals, *Solid State Commun.* 97 (1996) 1101–1104.
- [17] R. Robles, N. Barreau, A. Vega, S. Marsillac, J.C. Bernède, A. Mokrani, Optical properties of large band gap  $\beta$ -In<sub>2</sub>S<sub>3–3x</sub>O<sub>3x</sub> compounds obtained by physical vapor deposition, *Opt. Mater.* 27 (2005) 647.
- [18] K.M. Othonos, M. Zervos, C. Christofides, A. Othonos, Ultrafast spectroscopy and red emission from  $\beta$ -Ga<sub>2</sub>O<sub>3</sub>/β-Ga<sub>2</sub>S<sub>3</sub> nanowires, *Nanoscale Res. Lett.* 10 (2015) 304.
- [19] H.F. Liu, K.K.A. Antwi, N.L. Yakovlev, H.R. Tan, L.T. Ong, S.J. Chua, D.Z. Chi, Synthesis and phase evolutions in layered structure of Ga<sub>2</sub>S<sub>3</sub> semiconductor thin films on epitaxially GaAs (1 1 1) substrate, *ACS Appl. Mater. Interfaces* 6 (2014) 3501–3507.
- [20] N. Izu, W. Shin, N. Murayama, S. Kanzaki, Resistive oxygen gas sensors based on CeO<sub>2</sub> fine powder prepared using mist pyrolysis, *Sens. Actuators B* 87 (2002) 95–98.
- [21] G.Y. Chai, L. Chow, O. Lupan, E. Rusu, G.I. Stratan, H. Heinrich, V.V. Ursaki, I.M. Tiginyanu, Fabrication and characterization of an individual ZnO microwire-based UV photodetector, *Solid State Sci.* 13 (2011) 1250–1210.
- [22] C.H. Ho, C.C. Wu, Z.H. Cheng, Crystal structure and electronic structure of GaS<sub>1–x</sub>Se<sub>x</sub> series layered solids, *J. Cryst. Growth* 279 (2005) 321–328.
- [23] C.H. Ho, Enhanced photoelectric-conversion yield in niobium-incorporated In<sub>2</sub>S<sub>3</sub> with intermediate band, *J. Mater. Chem.* 21 (2011) 10518–10524.
- [24] G.A. Horley, P. O'Brien, J.-H. Park, A.J.P. White, D.J. Williams, Deposition of tetragonal  $\beta$ -In<sub>2</sub>S<sub>3</sub> thin films from tris(*N,N*-diisopropylmonothiocarbamate) indium(III), In (SOCN<sup>+</sup>Pr<sub>2</sub>)<sub>3</sub>, by low pressure metal-organic chemical vapor deposition, *J. Mater. Chem.* 9 (1999) 1289–1292.
- [25] R. Lucena, I. Aguilera, P. Palacios, P. Wahnón, J.C. Conesa, Synthesis and spectral properties of nanocrystalline V-substituted In<sub>2</sub>S<sub>3</sub>, a novel material for more efficient use of solar radiation, *Chem. Mater.* 20 (2008) 5125–5127.
- [26] M.P. Pardo, M. Guittard, A. Chlouet, A. Tomas, Diagramme de phases gallium-soufre et études structurales des phases soildes, *J. Soild State Chem.* 102 (1993) 423–433.
- [27] M. Kraini, N. Bouguila, I. Halidou, A. Moadhen, C. Vázquez-Vázquez, M.A. López-Quintela, S. Alaya, Study of optical and electrical properties of In<sub>2</sub>S<sub>3</sub>:Sn films deposited by spray pyrolysis, *J. Electron. Mater.* 44 (2015) 2536–2543.
- [28] G. Lucazeau, J. Leory, Etude vibrationnelle de  $\alpha$  Ga<sub>2</sub>S<sub>3</sub>, *Spectrochim. Acta* 34A (1978) 29–32.
- [29] C. Julien, S. Barnier, I. Ivanov, M. Guittard, M.P. Pardo, A. Chlouet, Vibrational studies of copper thiogallate solid solutions, *Mater. Sci. Eng. B* 57 (1999) 102–109.
- [30] C.H. Ho, Y.C. Chen, Thickness-tunable band gap modulation in  $\gamma$ -In<sub>2</sub>Se<sub>3</sub>, *RSC Adv.* 3 (2013) 24896–24899.
- [31] D.E. Aspnes, Handbook on Semiconductors, in: M. Balkanski (Ed.), North Holland Amsterdam, 1980, p.109.
- [32] C.H. Ho, H.H. Chen, Optically decomposed near-band-edge structure and excitonic transitions in Ga<sub>2</sub>S<sub>3</sub>, *Sci. Rep.* 4 (2014) 06143.
- [33] M.J. Zhang, X.M. Jiang, L.J. Zhou, G.C. Guo, Two phases of Ga<sub>2</sub>S<sub>3</sub>: promising infrared second-order nonlinear optical materials with very high laser induced damage thresholds, *J. Mater. Chem. C* 1 (2013) 4754–4760.
- [34] C.H. Ho, C.H. Chan, L.C. Tien, Y.S. Huang, Direct optical observation of band edge excitons, band gap and Fermi level in degenerate semiconducting oxide nanowires In<sub>2</sub>O<sub>3</sub>, *J. Phys. Chem. C* 115 (2011) 25088–25096.
- [35] C.H. Ho, M.H. Lin, C.C. Pan, Optical-memory switching and oxygen detection based on the CVT grown  $\gamma$ - and  $\alpha$ -phase In<sub>2</sub>Se<sub>3</sub>, *Sens. Actuators B* 209 (2015) 811–819.
- [36] J.S. Lee, Y.H. Won, H.N. Kim, C.D. Kim, W.T. Kim, Photoluminescence of Ga<sub>2</sub>S<sub>3</sub> and Ga<sub>2</sub>S<sub>3</sub>:Mn single crystals, *Solid State Commun.* 97 (1996) 1101–1104.

## Biographies

**Ching-Hwa Ho** is now a distinguished professor in National Taiwan University of Science and Technology (Taiwan Tech) Taipei, Taiwan. He received his BS degree in the Electronic Department from National Taiwan Institute of Technology in 1989, and the MS degree from the same department in 1991. In 1999, he received a PhD in the Electronic-Engineering Department from National Taiwan University of Science and Technology. He served as a full professor in the Graduate Institute of Applied Science and Technology since 2009. Professor Ho's research interests are chalcogenides energy compounds, measurement science and technology, and optoelectronic materials and devices. He has authored and co-authored more than 130 journal papers in his related research fields.

**Min-Han Lin** received his MS degree in the China University of Science and Technology and he got into the PhD program in the National Taiwan University of Science and Technology in 2013. His research correlated with III–VI indium selenide, indium oxide, II–VI ZnS and spectroscopy of semiconductors.

**Yi-Ping Wang** received his PhD degree from the Electronic Department in National Taiwan University of Science and Technology in 2013. His research interest was focused on semiconductor thin film and bulk metal chalcogenides including crystal growth and characterization.

**Ying-Sheng Huang** was a chair professor in both the Electronic Department and Institute of Electro-Optical Engineering in the National Taiwan University of Science and Technology. Professor Huang's research interest focused on single-crystal growth of transition-metal chalcogenides (especially on 2D layered crystal and oxide nanostructures) and their physical and chemical properties. He has co-authored more than 350 journal papers in his related research fields.